



Article

Growth Process and CQDs-modified $\text{Bi}_4\text{Ti}_3\text{O}_{12}$ Square Plates with Enhanced Photocatalytic Performance

Xinxin Zhao ¹, Hua Yang ^{1,*} , Ziming Cui ¹, Xiangxian Wang ¹ and Zao Yi ²

¹ State Key Laboratory of Advanced Processing and Recycling of Non-ferrous Metals, Lanzhou University of Technology, Lanzhou 730050, China; zhaoxinxin7520@163.com (X.Z.); cuizim1983@163.com (Z.C.); wangxx869@126.com (X.W.)

² Joint Laboratory for Extreme Conditions Matter Properties, Southwest University of Science and Technology, Mianyang 621010, China; yizaomy@swust.edu.cn

* Correspondence: hyang@lut.cn; Tel.: +86-931-297-3783

Received: 27 December 2018; Accepted: 16 January 2019; Published: 18 January 2019



Abstract: $\text{Bi}_4\text{Ti}_3\text{O}_{12}$ square plates were synthesized via a hydrothermal route, and their growth process was systematically investigated. Carbon quantum dots (CQDs) were prepared using glucose as the carbon source, which were then assembled on the surface of $\text{Bi}_4\text{Ti}_3\text{O}_{12}$ square plates via a hydrothermal route with the aim of enhancing the photocatalytic performance. XRD (X-ray powder diffraction), SEM (scanning electron microscopy), TEM (transmission electron microscopy), UV-vis DRS (diffuse reflectance spectroscopy), XPS (X-ray photoelectron spectroscopy), FTIR (Fourier transform infrared spectroscopy), PL (photoluminescence) spectroscopy, EIS (electrochemical impedance spectroscopy) and photocurrent spectroscopy were used to systematically characterize the as-prepared samples. It is demonstrated that the decoration of CQDs on $\text{Bi}_4\text{Ti}_3\text{O}_{12}$ plates leads to an increased visible light absorption, slightly increased bandgap, increased photocurrent density, decreased charge-transfer resistance, and decreased PL intensity. Simulated sunlight and visible light were separately used as a light source to evaluate the photocatalytic activity of the samples toward the degradation of RhB in aqueous solution. Under both simulated sunlight and visible light irradiation, CQDs@ $\text{Bi}_4\text{Ti}_3\text{O}_{12}$ composites with an appropriate amount of CQDs exhibit obviously enhanced photocatalytic performance. However, the decoration of excessive CQDs gives rise to a decrease in the photocatalytic activity. The enhanced photocatalytic activity of CQDs-modified $\text{Bi}_4\text{Ti}_3\text{O}_{12}$ can be attributed to the following reasons: (1) The electron transfer between $\text{Bi}_4\text{Ti}_3\text{O}_{12}$ and CQDs promotes an efficient separation of photogenerated electron/hole pairs in $\text{Bi}_4\text{Ti}_3\text{O}_{12}$; (2) the up-conversion photoluminescence emitted from CQDs could induce the generation of additional electron/hole pairs in $\text{Bi}_4\text{Ti}_3\text{O}_{12}$; and (3) the photoexcited electrons in CQDs could participate in the photocatalytic reactions.

Keywords: $\text{Bi}_4\text{Ti}_3\text{O}_{12}$ square plates; CQDs; CQDs@ $\text{Bi}_4\text{Ti}_3\text{O}_{12}$ composites; photodegradation of RhB; photocatalytic mechanism

1. Introduction

To date, water pollution particularly caused by organic dyes and pigments generated from chemical industries is getting increasingly serious and poses a great threat to aquatic life and human health. In the context of energy shortage, how to use solar energy as the power source to deal with water pollution has become an important subject. To achieve this aim, recently, semiconductor-based photocatalysis has aroused tremendous interest [1–6]. Titanium dioxide and titanium-based oxide semiconductors have been extensively studied as an important class of semiconductor photocatalysts.

Nevertheless, these semiconductor photocatalysts generally have a wide bandgap (E_g) greater than 3.0 eV and are photocatalytically active only under ultraviolet (UV) irradiation. This limits the utilization rate of solar energy. Furthermore, the photoexcited electrons (e^-) and holes (h^+) in the semiconductors easily undergo rapid geminate recombination, and thus, only a small fraction of the photoexcited carriers are able to participate in the photocatalytic reactions. This implies that the photon utilization rate is very low. Widening the light absorption range and promoting the photoexcited electron/hole pair separation are two of the key points to achieve an excellent photocatalyst with the best use of solar energy. Therefore, many strategies have been developed to modify semiconductor photocatalysts [7–16].

Low-dimension nanomaterials like graphene, carbon quantum dots (CQDs) and SiC nanowires offer great potential applications for biological labeling, bioimaging, drug delivery, energy conversion, optoelectronic devices, wave absorption and sensors due to their attractive properties [17–28]. In particular, photoexcited CQDs are excellent electron donors and electron acceptors. The interesting photoinduced electron transfer property suggests that CQDs can be used to modify photocatalysts with the aim of promoting the separation of photogenerated electron/hole pairs. Moreover, the PL up-conversion effect allows CQDs to harvest long-wavelength light (visible/near-infrared (vis/NIR) light) and then emit short-wavelength light (UV light). The emitted UV light can stimulate the generation of electron/hole pairs in wide-bandgap semiconductors like titanium-based oxides. Assembly of CQDs on the surface of semiconductors has become an important strategy for the design of excellent semiconductor photocatalysts capable of making full use of solar energy. Several examples of CQDs-modified photocatalysts with enhanced photocatalytic performance include CQDs/ Bi_2WO_6 , $\alpha\text{-Bi}_2\text{O}_3$ /C-dots, CQDs/ BiOBr , and CQDs/g- C_3N_4 [29–32].

As an important titanium-based oxide semiconductor, bismuth titanate ($\text{Bi}_4\text{Ti}_3\text{O}_{12}$) has been extensively studied owing to its pronounced photocatalytic activity toward the degradation of organic pollutants and water splitting into hydrogen [33–37]. $\text{Bi}_4\text{Ti}_3\text{O}_{12}$ is composed of perovskite-like $(\text{Bi}_2\text{Ti}_3\text{O}_{10})^{2-}$ blocks regularly interleaved with $(\text{Bi}_2\text{O}_2)^{2+}$ units, forming a special layer structure along the [010] direction (b-axis) [38]. A polarization electric field is formed perpendicular to the (010) facet. Under the action of the polarization electric field, photogenerated electrons and holes are easily separated and migrate along the [010] direction to reach the (010) facet [39]. The anisotropic layered structure suggests that the photocatalytic activity of $\text{Bi}_4\text{Ti}_3\text{O}_{12}$ highly depends on its morphology. In our previous work, we synthesized large-sized $\text{Bi}_4\text{Ti}_3\text{O}_{12}$ nanosheets with a highly exposed (010) facet via a hydrothermal route and found that their photocatalytic activity was much higher than that of $\text{Bi}_4\text{Ti}_3\text{O}_{12}$ nanoparticles [33]. On the other hand, $\text{Bi}_4\text{Ti}_3\text{O}_{12}$ was frequently integrated with other semiconductors or decorated with noble metals to achieve excellent composite photocatalysts [40–48]. Very recently, Wang et al. reported on bamboo prepared CQDs for enhancing $\text{Bi}_4\text{Ti}_3\text{O}_{12}$ photocatalytic activity [49]. Their work demonstrated that CQDs were a good modifier to enhance the photocatalytic activity of $\text{Bi}_4\text{Ti}_3\text{O}_{12}$, although only 65% of ciprofloxacin was observed to be degraded at 90 min of photocatalysis. Further increasing the photocatalytic performance and elucidating the enhanced photocatalytic mechanism of CQDs-modified $\text{Bi}_4\text{Ti}_3\text{O}_{12}$ is still necessary. Here we report on an alternative method to assemble CQDs on $\text{Bi}_4\text{Ti}_3\text{O}_{12}$ square plates. In the present study, glucose was used as the carbon source to produce CQDs. The preparation of CQDs and $\text{Bi}_4\text{Ti}_3\text{O}_{12}$ square plates as well as the assembly of CQDs on $\text{Bi}_4\text{Ti}_3\text{O}_{12}$ were carried out via a hydrothermal route. Moreover, the growth process of $\text{Bi}_4\text{Ti}_3\text{O}_{12}$ square plates was systematically investigated. The characteristics, photocatalytic performance and photocatalytic mechanism of the as-prepared CQDs/ $\text{Bi}_4\text{Ti}_3\text{O}_{12}$ composites were systematically investigated and discussed.

2. Materials and Methods

2.1. Synthesis of $\text{Bi}_4\text{Ti}_3\text{O}_{12}$ Square Plates

A hydrothermal route was used to synthesize $\text{Bi}_4\text{Ti}_3\text{O}_{12}$ square plates. In a typical synthesis, 0.004 mol (1.9402 g) of $\text{Bi}(\text{NO}_3)_3 \cdot 5\text{H}_2\text{O}$ was dissolved in 20 mL of 10% v/v dilute nitric acid solution (solution A), 0.003 mol (0.5691 g) of TiCl_4 was dissolved in 20 mL of deionized water (solution B), and 0.2 mol (8 g) of NaOH was dissolved in 40 mL of deionized water (solution C). The solutions B and C were successively dropped in the solution A slowly with the aid of mild magnetic stirring. The resultant mixture was loaded and sealed into a 100 mL Teflon-lined stainless steel autoclave and subjected to heat treatment at 200 °C. To investigate the growth process of $\text{Bi}_4\text{Ti}_3\text{O}_{12}$ square plates, different heat treatment temperatures (3, 6, 12, 24 and 36 h) were carried out. After the autoclave was naturally cooled to room temperature, the produced precipitate was collected by centrifugation, washed several times with deionized water and absolute ethanol, and dried at 60 °C for 12 h.

2.2. Assembly of CQDs on the Surface of $\text{Bi}_4\text{Ti}_3\text{O}_{12}$ Square Plates

$\text{Bi}_4\text{Ti}_3\text{O}_{12}$ square plates synthesized at 200 °C for 24 h via the above hydrothermal route were used to be decorated with CQDs in two steps. The first step was to prepare CQDs suspension using glucose as the carbon source. One gram of glucose was added to 80 mL deionized water, followed by ultrasonic treatment for 30 min and magnetic stirring for another 30 min. The glucose solution was then loaded into a Teflon-lined stainless steel autoclave (100 mL) and subjected to heat treatment at 180 °C for 4 h. After the autoclave was naturally cooled to room temperature, the solution was filtered through a millipore filter paper two times. The obtained reddish-brown solution was CQDs suspension. The second step was to assemble CQDs on the surface of $\text{Bi}_4\text{Ti}_3\text{O}_{12}$ square plates. In a typical assembly process, 0.1 g of $\text{Bi}_4\text{Ti}_3\text{O}_{12}$ plates was added into 70 mL of deionized water and ultrasonicated for 30 min. Ten milliliters of the CQDs suspension was added drop by drop into the $\text{Bi}_4\text{Ti}_3\text{O}_{12}$ suspension and magnetically stirred for 1 h. The resultant mixture was loaded into a 100 mL Teflon-lined stainless steel autoclave and subjected to heat treatment at 130 °C for 4 h. After cooling to room temperature naturally, the precipitate was collected by centrifugation and dried at 60 °C for 12 h. The final product was obtained as the CQDs@ $\text{Bi}_4\text{Ti}_3\text{O}_{12}$ composite. According to this procedure, several composite samples with different CQDs contents were prepared by adding different volumes of CQDs solution (5, 10, 15, and 20 mL) into the precursor $\text{Bi}_4\text{Ti}_3\text{O}_{12}$ suspension, and the corresponding samples were designated as 5CQDs@ $\text{Bi}_4\text{Ti}_3\text{O}_{12}$, 10CQDs@ $\text{Bi}_4\text{Ti}_3\text{O}_{12}$, 15CQDs@ $\text{Bi}_4\text{Ti}_3\text{O}_{12}$, and 20CQDs@ $\text{Bi}_4\text{Ti}_3\text{O}_{12}$.

2.3. Sample Characterization

The crystal structure of the samples was identified by x-ray powder diffraction (XRD) with Cu $K\alpha$ radiation ($\lambda = 0.15406$ nm) on a D8 Advance x-ray diffractometer (Bruker AXS, Karlsruhe, Germany). Scanning electron microscopy (SEM) and transmission electron microscopy (TEM) were used to investigate the morphology and microstructure of the samples. The SEM and TEM investigation was performed on a JSM-6701F scanning electron microscope (JEOL Ltd., Tokyo, Japan) and a JEM-1200EX transmission electron microscope (JEOL Ltd., Tokyo, Japan). Energy-dispersive x-ray spectroscopy (EDS) attached to TEM was used to analyze the chemical composition and elemental distribution of the samples. The optical absorption and bandgap energy of the samples were characterized by UV-vis diffuse reflectance spectroscopy (DRS) on a TU-1901 double beam UV-vis spectrophotometer (Beijing Purkinje General Instrument Co. Ltd., Beijing, China). X-ray photoelectron spectroscopy (XPS) measurement was carried out on a PHI-5702 multi-functional x-ray photoelectron spectrometer (Physical Electronics, hanhassen, MN, USA) to reveal the composition and chemical states of elements in the samples. Fourier transform infrared spectroscopy (FTIR) analysis was performed on a Spectrum Two FTIR spectrophotometer (PerkinElmer, Waltham, MA, USA) in the range of 500–4000 cm^{-1} using KBr powder. A RF-6000 fluorescence spectrophotometer (Shimadzu, Kyoto, Japan) was used to measure the photoluminescence (PL) spectra of the samples with an excitation wavelength of 320 nm.

2.4. Photocatalytic Testing

Simulated sunlight emitted by a 200 W xenon lamp ($300 < \lambda < 2500$ nm) and visible light generated by a 200 W halogen-tungsten lamp ($\lambda > 400$ nm) were separately used as the light source to evaluate the photocatalytic activity of the samples toward the degradation of rhodamine B (RhB) in aqueous solution. Such as in a typical photocatalytic experiment, 0.2 g of the photocatalyst was loaded into 100 mL of $5 \text{ mg}\cdot\text{L}^{-1}$ RhB aqueous solution. The mixture was put into the photoreactor and magnetically stirred in the dark for 30 min to determine the adsorption of RhB onto the photocatalyst surface. During the photocatalytic process, a circulating water cooling system was used to cool the photoreactor in order to maintain the reaction solution at room temperature (~ 21 °C). The residual concentration of RhB was monitored every 30 min. To achieve this, 2.5 mL of the reaction solution was sampled from the photoreactor and centrifugated to remove the photocatalyst. The residual concentration of RhB was determined by measuring the absorbance of the reaction solution on a UV-vis spectrophotometer at $\lambda = 554$ nm. The degradation percentage of RhB is defined as follows: $D\% = (1 - C_t/C_0) \times 100\%$, where C_0 and C_t represent the initial and residual RhB concentrations after photocatalysis for t min.

2.5. Electrochemical Measurement

A three-electrode cell configuration was used for the transient photocurrent response and electrochemical impedance spectroscopy (EIS) measurements of the samples on a CST 350 electrochemical workstation (Wuhan Corrtest Instruments Co. Ltd., Wuhan, China) [50,51]. A platinum foil electrode and a standard calomel electrode (SCE) were used as the counter electrode and reference electrode, respectively. The working electrode was prepared following the procedure described in the literature [51]. Stoichiometric amounts of the photocatalyst (15 mg), acetylene black (0.75 mg) and polyvinylidene fluoride (PVDF, 0.75 mg) were uniformly mixed into 1 mL 1-methyl-2-pyrrolidione (NMP) that acted as the dispersant. The paste mixture was homogeneously coated onto fluorine-doped tin oxide (FTO) glass substrate (effective area: $1 \times 1 \text{ cm}^2$). After drying at 60 °C for 5 h, the final working electrode was obtained. The electrolyte used in this study is a Na_2SO_4 aqueous solution with a concentration of $0.1 \text{ mol}\cdot\text{L}^{-1}$. Simulated sunlight emitted from a 200 W xenon lamp was used as the light source. The transient photocurrent response measurement was performed at a bias potential of 0.2 V. The EIS measurement was performed by imposing a small sinusoidal voltage of 5 mV amplitude over the frequency range from 100 kHz to 0.01 Hz. To investigate the flat band potential of $\text{Bi}_4\text{Ti}_3\text{O}_{12}$, the EIS was measured at different applied potentials in the dark.

3. Results and Discussion

3.1. Growth Process of $\text{Bi}_4\text{Ti}_3\text{O}_{12}$ Square Plates

Figure 1 shows the XRD patterns of $\text{Bi}_4\text{Ti}_3\text{O}_{12}$ samples prepared at 200 °C with different reaction times ($t = 3, 6, 12, 24,$ and 36 h). It is seen that the sample obtained at $t = 3$ h consists of a mixture of phases including $\text{Bi}_4\text{Ti}_3\text{O}_{12}$ (PDF#35-0795), Bi_2O_3 (PDF#27-0050) and anatase TiO_2 (PDF#21-1272). Moreover, a broad peak at around $2\theta = 10^\circ$ is observed on the XRD pattern, which arises from the amorphous $\text{Bi}(\text{OH})_3$ and $\text{Ti}(\text{OH})_4$ precipitates hydrolyzed from $\text{Bi}(\text{NO}_3)_3$ and TiCl_4 . When the reaction time is increased up to 6 h, the diffraction peaks related to Bi_2O_3 , TiO_2 and amorphous substances disappear. All the diffraction peaks can be indexed according to the standard diffraction pattern of PDF#35-0795, implying the formation of a single $\text{Bi}_4\text{Ti}_3\text{O}_{12}$ orthorhombic phase. With prolonging the reaction time, the prepared samples maintain a pure $\text{Bi}_4\text{Ti}_3\text{O}_{12}$ orthorhombic phase without the appearance of other impurities.

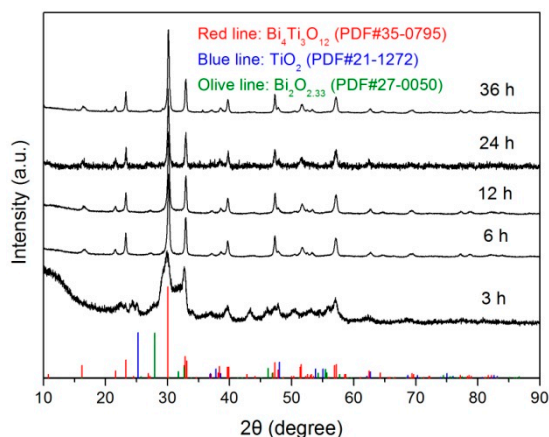


Figure 1. XRD patterns of $\text{Bi}_4\text{Ti}_3\text{O}_{12}$ samples prepared at $200\text{ }^\circ\text{C}$ with different reaction times ($t = 3, 6, 12, 24,$ and 36 h).

Figure 2 shows the SEM images of $\text{Bi}_4\text{Ti}_3\text{O}_{12}$ samples prepared at different reaction times ($t = 3, 6, 12, 24,$ and 36 h). As shown in Figure 2a, the product obtained at 3 h reaction time is composed of nanorods, spherical nanoparticles and amorphous aggregates, which are characterized as $\text{Bi}_4\text{Ti}_3\text{O}_{12}$, Bi_2O_3 , TiO_2 , and $\text{Bi}(\text{OH})_3/\text{Ti}(\text{OH})_4$ precipitates. At 6 h reaction time (Figure 2b), the $\text{Bi}_2\text{O}_3/\text{TiO}_2$ spherical nanoparticles and $\text{Bi}(\text{OH})_3/\text{Ti}(\text{OH})_4$ precipitates are crystallized into $\text{Bi}_4\text{Ti}_3\text{O}_{12}$ nanorods. With further increasing the reaction time up to 12 h (Figure 2c), the formed $\text{Bi}_4\text{Ti}_3\text{O}_{12}$ nanorods gradually grow into brick-like nanoparticles. When the reaction time is increased up to 24 h (Figure 2d,e), it brings about the synthesis of $\text{Bi}_4\text{Ti}_3\text{O}_{12}$ square plates with an average lateral size of $\sim 1\text{ }\mu\text{m}$ and thickness of $\sim 200\text{ nm}$. However, too long a reaction time leads to partial dissolution of the square plates into small-sized brick-like nanoparticles, as shown in Figure 2f.

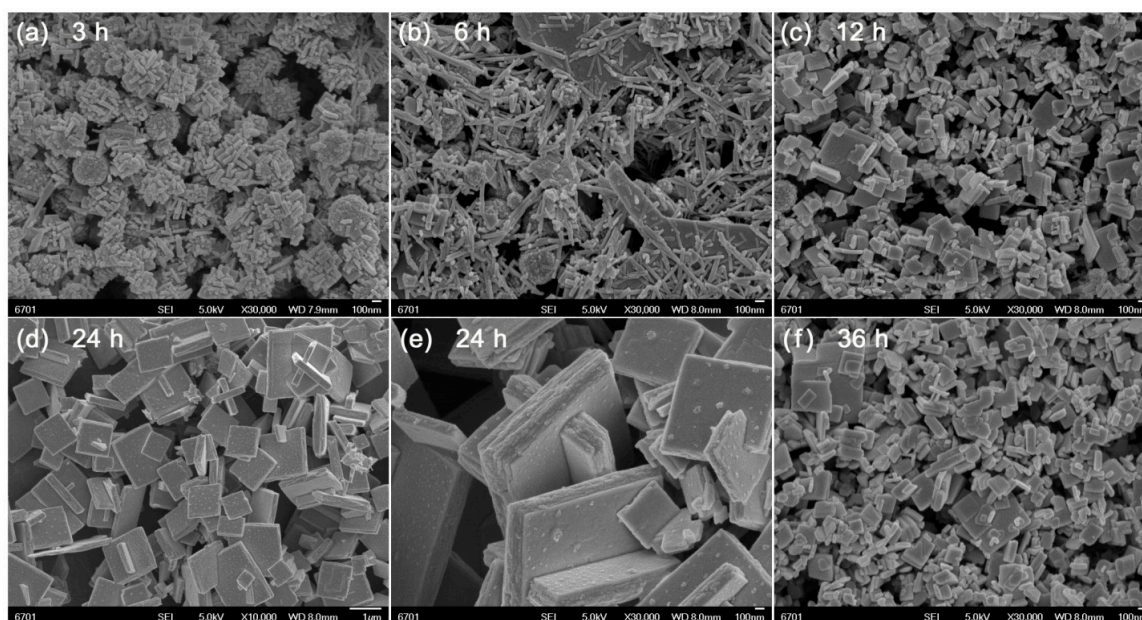


Figure 2. SEM images of $\text{Bi}_4\text{Ti}_3\text{O}_{12}$ samples prepared at different reaction times ($t = 3, 6, 12, 24,$ and 36 h).

Based on the XRD and SEM results, the formation process of $\text{Bi}_4\text{Ti}_3\text{O}_{12}$ square plates is schematically illustrated in Figure 3. The “dissolution–crystallization” mechanism can be used to describe the hydrothermal formation of $\text{Bi}_4\text{Ti}_3\text{O}_{12}$ square plates [52]. In the precursor solution, $\text{Bi}(\text{NO}_3)_3$ and TiCl_4 were hydrolyzed into $\text{Bi}(\text{OH})_3$ and $\text{Ti}(\text{OH})_4$ hydroxides with the aid of NaOH .

At high temperature and pressure environments, the $\text{Bi}(\text{OH})_3$ and $\text{Ti}(\text{OH})_4$ precipitates are to dissolve and form ion groups under the action of NaOH that serves as the mineralizer. In the locally formed supersaturated fluid region, $\text{Bi}_4\text{Ti}_3\text{O}_{12}$ nanorods are crystallized by nucleation, precipitation, dehydration, and growth. Simultaneously, Bi_2O_3 and TiO_2 could also be formed in this process. With the hydrothermal reaction going on, Bi_2O_3 and TiO_2 will dissolve again to form ion groups under the attack of NaOH , which will then subsequently crystallize into $\text{Bi}_4\text{Ti}_3\text{O}_{12}$ nanorods. The formation of $\text{Bi}_4\text{Ti}_3\text{O}_{12}$ crystals can be simply described by Equations (1) and (2). With increasing the reaction time, $\text{Bi}_4\text{Ti}_3\text{O}_{12}$ nanorods gradually grow into brick-like nanoparticles and then into square plates. The formation of $\text{Bi}_4\text{Ti}_3\text{O}_{12}$ square plates can be explained as a result of the reduction of the overall surface energy. It is noted that the growth process of $\text{Bi}_4\text{Ti}_3\text{O}_{12}$ square plates is simultaneously accompanied by their dissolution process. After a relatively long reaction time, the dissolution process could predominate over the growth process, and as a result, $\text{Bi}_4\text{Ti}_3\text{O}_{12}$ square plates are etched into small-sized brick-like nanoparticles.

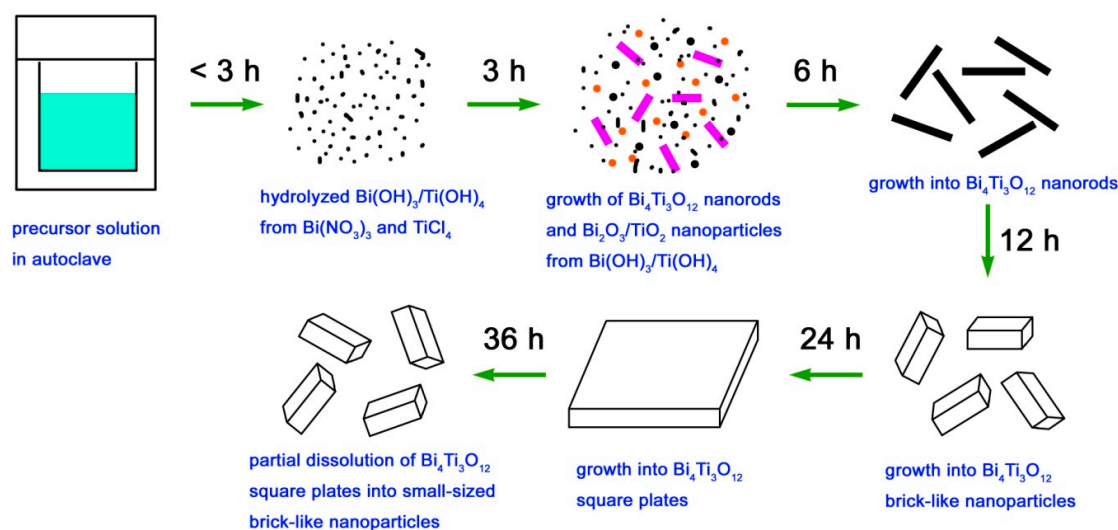
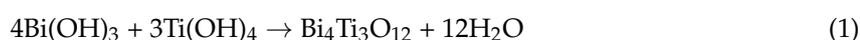


Figure 3. Schematic illustration of the formation process of $\text{Bi}_4\text{Ti}_3\text{O}_{12}$ square plates.

3.2. CQDs-modified $\text{Bi}_4\text{Ti}_3\text{O}_{12}$ Square Plates

The photocatalytic activity of the as-prepared $\text{CQDs}@ \text{Bi}_4\text{Ti}_3\text{O}_{12}$ composites was evaluated by the degradation of RhB in aqueous solution separately under the irradiation of simulated sunlight ($300 < \lambda < 2500 \text{ nm}$) and visible light ($\lambda > 400 \text{ nm}$). Before the photocatalytic degradation experiment, the adsorption of RhB onto bare $\text{Bi}_4\text{Ti}_3\text{O}_{12}$ and $\text{CQDs}@ \text{Bi}_4\text{Ti}_3\text{O}_{12}$ composites was measured in the dark at 30 min of contact time and is obtained as 3.5–15.3%. It is observed that the RhB adsorption gradually increases with increasing the CQDs content, which is ascribed to the enhanced dye adsorption of CQDs. Generally, an appropriate increase in the dye adsorption is conducive to photocatalysis. The time-dependent photocatalytic degradation of RhB under simulated sunlight irradiation is shown in Figure 4a. The degradation percentage of RhB after 120 min of photocatalysis is given in Table 1. It is seen that the decoration of an appropriate amount of CQDs on $\text{Bi}_4\text{Ti}_3\text{O}_{12}$ leads to a significantly enhanced photocatalytic activity. The highest photocatalytic performance is observed for the $10\text{CQDs}@ \text{Bi}_4\text{Ti}_3\text{O}_{12}$ composite prepared by adding 10 mL CQDs solution, and the degradation percentage of RhB reaches 94.3%. However, decoration of excessive CQDs on $\text{Bi}_4\text{Ti}_3\text{O}_{12}$ could reduce the light absorption of $\text{Bi}_4\text{Ti}_3\text{O}_{12}$, and thus, give rise to a decrease in the photocatalytic activity.

To further compare the photocatalytic activity between the samples, the degradation kinetics of RhB were investigated. As shown in Figure 4b, the plots of $\ln(C_t/C_0)$ vs irradiation time t can be well modeled using the pseudo-first-order kinetic equation: $\ln(C_t/C_0) = -k_{app}t$, where k_{app} is the apparent first-order reaction rate constant [53]. The obtained value of k_{app} from the slope of the regression lines is given in Table 1. It is seen that the optimal composite 10CQDs@Bi₄Ti₃O₁₂ manifests a photocatalytic activity ca. 1.8 times higher than that of bare Bi₄Ti₃O₁₂. Figure 4c shows the visible-light photocatalytic degradation of RhB over bare Bi₄Ti₃O₁₂ and CQDs@Bi₄Ti₃O₁₂ composites, and Figure 4d presents the plots of $\ln(C_t/C_0)$ vs irradiation time t . The obtained degradation percentage after photocatalytic reaction for 120 min and reaction rate constant k_{app} are summarized in Table 1. Photocatalyzed by bare Bi₄Ti₃O₁₂, only 15.7% of the dye is observed to be degraded, which is mainly ascribed to the dye adsorption and dye-photosensitized degradation. This indicates that bare Bi₄Ti₃O₁₂ exhibits poor photocatalytic activity under visible light irradiation. When compared with bare Bi₄Ti₃O₁₂, the CQDs@Bi₄Ti₃O₁₂ composites manifest a greatly enhanced visible-light photocatalytic activity. In particular, the 15CQDs@Bi₄Ti₃O₁₂ composite photocatalyzes 42.4% removal of the dye and displays a photocatalytic activity ca. 3.2 times as large as that of bare Bi₄Ti₃O₁₂ according to the reaction rate constants.

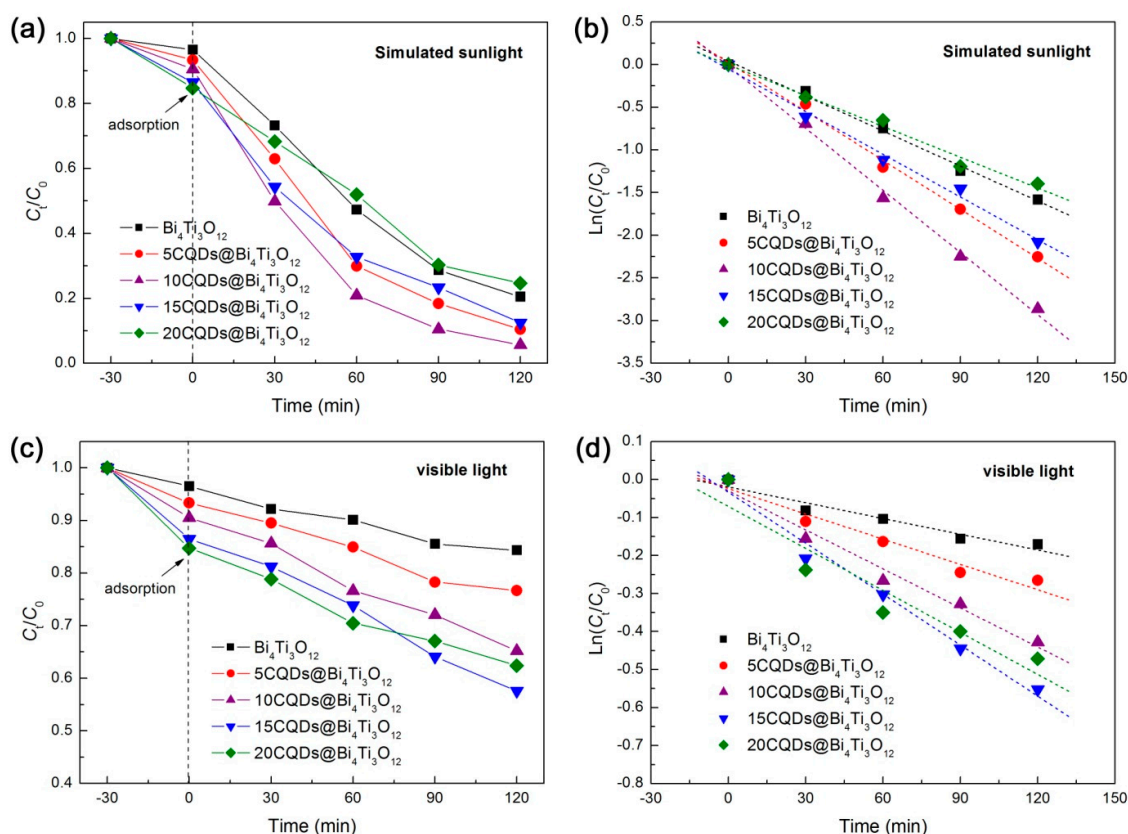


Figure 4. (a) Time-dependent photocatalytic degradation of RhB over Bi₄Ti₃O₁₂ and CQDs@Bi₄Ti₃O₁₂ composites with different CQDs contents under simulated sunlight irradiation. (b) Degradation kinetic plots of RhB over the samples under simulated sunlight irradiation. (c) Time-dependent photocatalytic degradation of RhB over the samples under visible light irradiation. (d) Degradation kinetic plots of RhB over the samples under visible light irradiation.

Table 1. Degradation percentage of RhB (reaction for 120 min) and apparent first-order reaction rate constant k_{app} for $\text{Bi}_4\text{Ti}_3\text{O}_{12}$ and $\text{CQDs@Bi}_4\text{Ti}_3\text{O}_{12}$ composites under irradiation of simulated sunlight and visible light.

Samples	Simulated Sunlight		Visible Light	
	Degradation (%)	k_{app} (min^{-1})	Degradation (%)	k_{app} (min^{-1})
$\text{Bi}_4\text{Ti}_3\text{O}_{12}$	79.5	0.01368	15.7	0.00139
5CQDs@ $\text{Bi}_4\text{Ti}_3\text{O}_{12}$	89.5	0.01912	23.3	0.00222
10CQDs@ $\text{Bi}_4\text{Ti}_3\text{O}_{12}$	94.3	0.02426	34.8	0.00342
15CQDs@ $\text{Bi}_4\text{Ti}_3\text{O}_{12}$	87.5	0.01667	42.4	0.00447
20CQDs@ $\text{Bi}_4\text{Ti}_3\text{O}_{12}$	75.3	0.01203	37.6	0.00368

Further investigation was specially carried out on the 10CQDs@ $\text{Bi}_4\text{Ti}_3\text{O}_{12}$ composite prepared with 10 mL CQDs solution with the aim of revealing its microstructure and enhanced photocatalytic mechanism. Figure 5a–c shows the TEM images of 10CQDs@ $\text{Bi}_4\text{Ti}_3\text{O}_{12}$. It is seen that $\text{Bi}_4\text{Ti}_3\text{O}_{12}$ has a geometrical morphology of square plates. Occasionally, the square plates are assembled into a T-shape structure, as shown in Figure 5b. Figure 5d shows the selected area electron diffraction (SAED) pattern obtained from the $\text{Bi}_4\text{Ti}_3\text{O}_{12}$ square plate of Figure 5c. The diffraction spots are regularly and periodically arranged, which can be indexed to the [010] zone axis of $\text{Bi}_4\text{Ti}_3\text{O}_{12}$ orthorhombic structure. The a-axis and b-axis are parallel to the lateral side of the square plate. The highly exposed plane of the square plate is identified to be the (010) facet. This crystallographic orientation of the $\text{Bi}_4\text{Ti}_3\text{O}_{12}$ square plate is further confirmed by the high resolution TEM (HRTEM) image, as shown in Figure 5e. The lattice fringes with d-spacing of 0.384 nm are observed to be parallel or perpendicular to the diagonal direction of the square plate and match well with the (202) crystal plane of $\text{Bi}_4\text{Ti}_3\text{O}_{12}$ orthorhombic phase. Although the TEM/HRTEM images and SAED pattern cannot show the presence of CQDs on $\text{Bi}_4\text{Ti}_3\text{O}_{12}$ plates, other methods can be used to determine the formation of CQDs@ $\text{Bi}_4\text{Ti}_3\text{O}_{12}$ composites. Figure 5f shows the dark-field scanning TEM (DF-STEM) image of the 10CQDs@ $\text{Bi}_4\text{Ti}_3\text{O}_{12}$ composite, and Figure 5g–j presents the corresponding energy-dispersive x-ray elemental mapping images of the region marked by the orange rectangle in Figure 5f. Besides the elements of Bi, Ti and O which constitute $\text{Bi}_4\text{Ti}_3\text{O}_{12}$ square plates, C element is also observed to be uniformly distributed throughout the plates. The elemental mapping images confirm the uniform assembly of CQDs on the surface of $\text{Bi}_4\text{Ti}_3\text{O}_{12}$ plates. The chemical composition of 10CQDs@ $\text{Bi}_4\text{Ti}_3\text{O}_{12}$ was further investigated by EDS spectrum, as shown in Figure 5k. It is obvious that the 10CQDs@ $\text{Bi}_4\text{Ti}_3\text{O}_{12}$ sample is composed of Bi, Ti, O, and C elements. The observed Cu signal on the EDS spectrum could arise from the microgrid used for supporting the sample in the TEM experiment [54]. The Bi/Ti atomic ratio obtained from the EDS spectrum is very close to that in the $\text{Bi}_4\text{Ti}_3\text{O}_{12}$ phase. However, the EDS spectrum shows a lower O content with respect to oxygen in $\text{Bi}_4\text{Ti}_3\text{O}_{12}$, which could be ascribed to non-sensitivity of EDS to light elements like O [54].

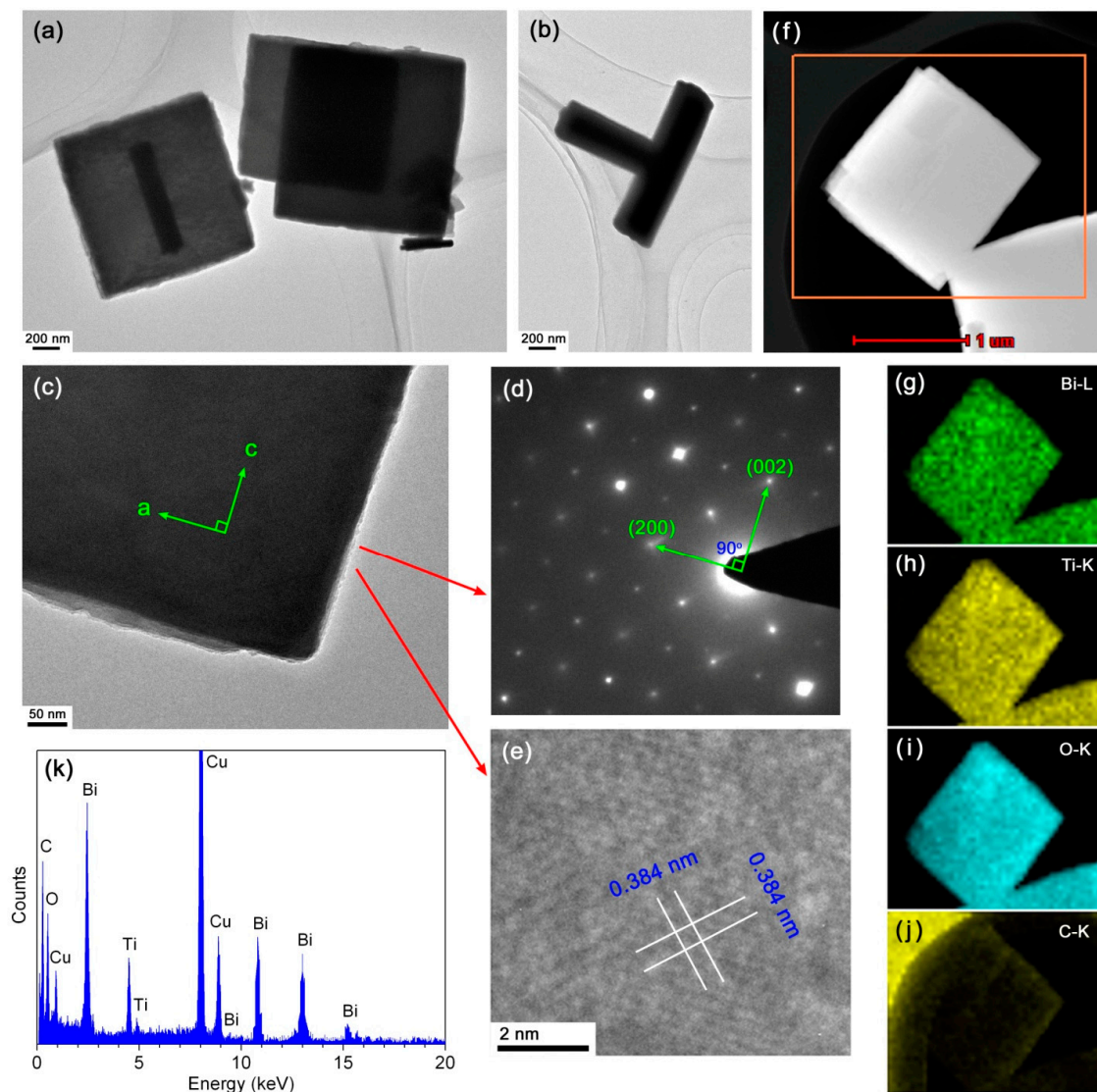


Figure 5. (a–c) TEM images of 10CQDs@Bi₄Ti₃O₁₂. (d) and (e) SAED pattern and HRTEM image obtained from the Bi₄Ti₃O₁₂ square plate of (c), respectively. (f) DF-STEM image of 10CQDs@Bi₄Ti₃O₁₂. (g–j) The corresponding energy-dispersive x-ray elemental mapping images of the region marked by orange rectangle in (f). (k) EDS spectrum of 10CQDs@Bi₄Ti₃O₁₂.

Figure 6 shows the XRD patterns of Bi₄Ti₃O₁₂ and 10CQDs@Bi₄Ti₃O₁₂. It is seen that the diffraction peaks of 10CQDs@Bi₄Ti₃O₁₂ are very similar to those of bare Bi₄Ti₃O₁₂, implying that Bi₄Ti₃O₁₂ undergoes no structural change when assembled with CQDs. No obvious diffraction signals assignable to CQDs are detected in the XRD pattern. The possible reason may be that CQDs have extremely weak x-ray diffraction due to the lack of long-range-ordered structure, and moreover, CQDs account for only a small fraction of the total mass of the 10CQDs@Bi₄Ti₃O₁₂ composite.

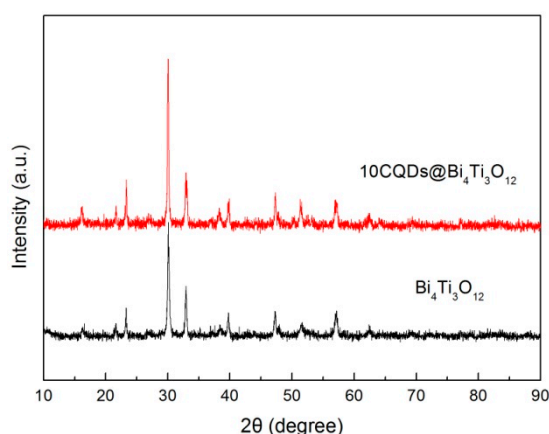


Figure 6. XRD patterns of $\text{Bi}_4\text{Ti}_3\text{O}_{12}$ and $10\text{CQDs}@Bi_4Ti_3O_{12}$.

Figure 7a,b shows the UV-vis DRS spectra of $\text{Bi}_4\text{Ti}_3\text{O}_{12}$ and $10\text{CQDs}@Bi_4Ti_3O_{12}$. A significantly enhanced light absorption in the wavelength range of 400–850 nm is observed for the $10\text{CQDs}@Bi_4Ti_3O_{12}$ composite when compared with bare $\text{Bi}_4Ti_3O_{12}$. The digital images of the samples separately inserted in Figure 7a,b demonstrate that bare $\text{Bi}_4Ti_3O_{12}$ is cream white, whereas $10\text{CQDs}@Bi_4Ti_3O_{12}$ manifests a gray color. The deepening of the apparent color for $10\text{CQDs}@Bi_4Ti_3O_{12}$ further confirms its enhanced visible-light absorption. This implies that the composite can make more efficient utilization of sunlight during photocatalysis. The first derivative curves of the UV-vis DRS spectra are used to determine the absorption edge of the samples [55]. As seen from Figure 7a,b, $\text{Bi}_4Ti_3O_{12}$ and $10\text{CQDs}@Bi_4Ti_3O_{12}$ exhibit an absorption edge of 372.2 and 364.4 nm, respectively. Based on the absorption edge, the bandgap energy (E_g) can be derived from the relationship $E_g = 1240/\lambda_{\text{abs}}$ (λ_{abs} represents the absorption edge wavelength), and is obtained as 3.33 eV for bare $\text{Bi}_4Ti_3O_{12}$ and 3.40 eV for $10\text{CQDs}@Bi_4Ti_3O_{12}$. The slight increase in the E_g of the composite could be ascribed to the interaction between $\text{Bi}_4Ti_3O_{12}$ plates and CQDs.

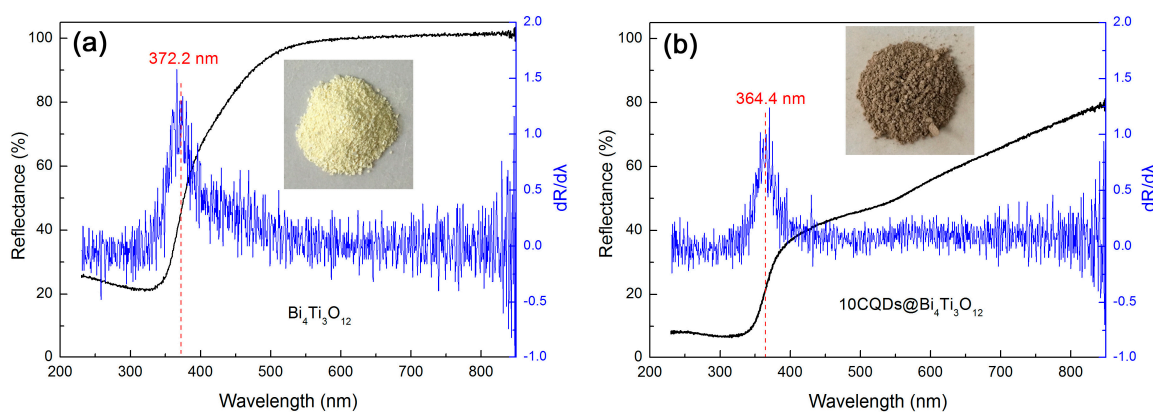


Figure 7. UV-vis DRS spectra, first derivative curves of the UV-vis DRS spectra and digital images of (a) $\text{Bi}_4\text{Ti}_3\text{O}_{12}$ and (b) $10\text{CQDs}@Bi_4Ti_3O_{12}$.

XPS analysis was carried out to reveal the composition and element chemical states of the $10\text{CQDs}@Bi_4Ti_3O_{12}$ composite. Figure 8a shows the XPS survey scan spectrum, revealing the existence of Bi, Ti, O, and C elements in the composite. Figure 8b–e illustrates the high resolution XPS spectra of Bi 4f, Ti 2p, O 1s, and C 1s, respectively. As seen from Figure 8b, the Bi 4f XPS spectrum shows two sharp peaks at 158.9 and 164.2 eV, which are attributed to the Bi 4f_{7/2} and Bi 4f_{5/2} binding energies, respectively [33,56,57]. The Ti 2p XPS spectrum shown in Figure 8c can be deconvoluted into three peaks at 457.9, 463.5 and 465.9 eV, which correspond to the binding energies of Ti 2p_{3/2}, Ti 2p_{1/2} and Bi 4d_{3/2} respectively [56,57]. The Bi 4f and Ti 2p binding energy peaks suggest that bismuth species

exists in +3 oxidation state and titanium species exhibits +4 oxidation state. The existence of other oxidation states can be excluded since no additional binding energy peaks are detected on the Bi 4f and Ti 2p XPS spectra. On the O 1s XPS spectrum (Figure 8d), the binding energy at 529.7 eV is attributed to the crystal lattice oxygen of $\text{Bi}_4\text{Ti}_3\text{O}_{12}$, whereas the binding energy at 531.5 eV could arise from chemisorbed oxygen species [58,59]. The C 1s XPS spectrum (Figure 8e) presents two peaks at 284.8 and 287.7 eV. The peak at 284.8 eV arises from the C–C sp^2 -hybridized carbon of CQDs and adventitious carbon that is used to calibrate the binding energy scale [59,60]. The peak at 287.7 eV is attributed to the presence of C–O–C or C=O [60].

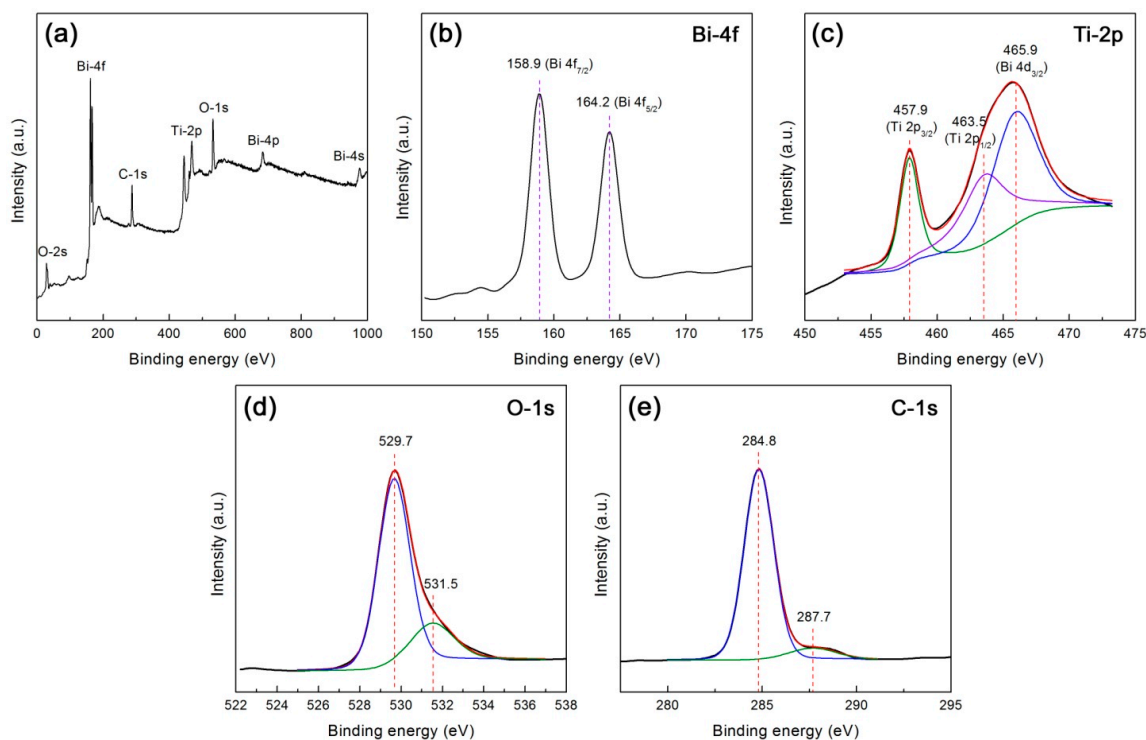


Figure 8. XPS spectra of 10CQDs@ $\text{Bi}_4\text{Ti}_3\text{O}_{12}$. (a) Survey scan spectrum; (b)–(e) High resolution XPS spectra of Bi 4f, Ti 2p, O 1s, and C 1s, respectively.

The functional groups of $\text{Bi}_4\text{Ti}_3\text{O}_{12}$ and 10CQDs@ $\text{Bi}_4\text{Ti}_3\text{O}_{12}$ were analyzed by FTIR spectra, as shown in Figure 9a. The broad bands detected at 3430 and 1637 cm^{-1} correspond to the stretching and bending vibrations of water molecules absorbed on the surface of the samples, respectively [61]. The peaks observed at 1102 and 1395 cm^{-1} account for the C–OH stretching and O–H in-plane deformation vibrations of alcohols left on the samples during their washing process. The broad absorption band at around 3146 cm^{-1} is assigned to the N–H stretching vibration of the NH_3^+ group [62]. The strong peak at 477 cm^{-1} and weak peak at 586 cm^{-1} are characterized as the Ti–O stretching vibration. The characteristic stretching vibration of Bi–O is observed at 819 cm^{-1} [63,64]. This implies the formation of the $\text{Bi}_4\text{Ti}_3\text{O}_{12}$ orthorhombic phase and its crystal structure undergoes no destruction when decorated with CQDs. Additional peaks at 638, 1270, 1467, and 1620 cm^{-1} are detected for the 10CQDs@ $\text{Bi}_4\text{Ti}_3\text{O}_{12}$ composite. The former two peaks (638 and 1270 cm^{-1}) are ascribed to the C–H deformation vibration and the latter two peaks (1467 and 1620 cm^{-1}) can be attributed to the C–C stretching vibration [65]. These absorption peaks suggest that CQDs are assembled on the surface of $\text{Bi}_4\text{Ti}_3\text{O}_{12}$ plates.

To reveal the separation and transfer behavior of photogenerated electrons and holes, PL, photocurrent response and EIS analyses were carried out. Figure 9b shows the PL spectra of $\text{Bi}_4\text{Ti}_3\text{O}_{12}$ and 10CQDs@ $\text{Bi}_4\text{Ti}_3\text{O}_{12}$ measured at an excitation wavelength of 320 nm. Both samples clearly display the PL emission peaks at 448, 466, 480, and 491 nm, which arise due to the recombination of

photogenerated electron/hole pairs. When compared with bare $\text{Bi}_4\text{Ti}_3\text{O}_{12}$, the $10\text{CQDs}@ \text{Bi}_4\text{Ti}_3\text{O}_{12}$ composite exhibits the PL emission peaks with relatively lower intensity, implying a decreased electron/hole recombination. The efficient separation of electron/hole pairs occurring in the composite can be explained as a result of the electron transfer from the conduction band (CB) of $\text{Bi}_4\text{Ti}_3\text{O}_{12}$ to CQDs.

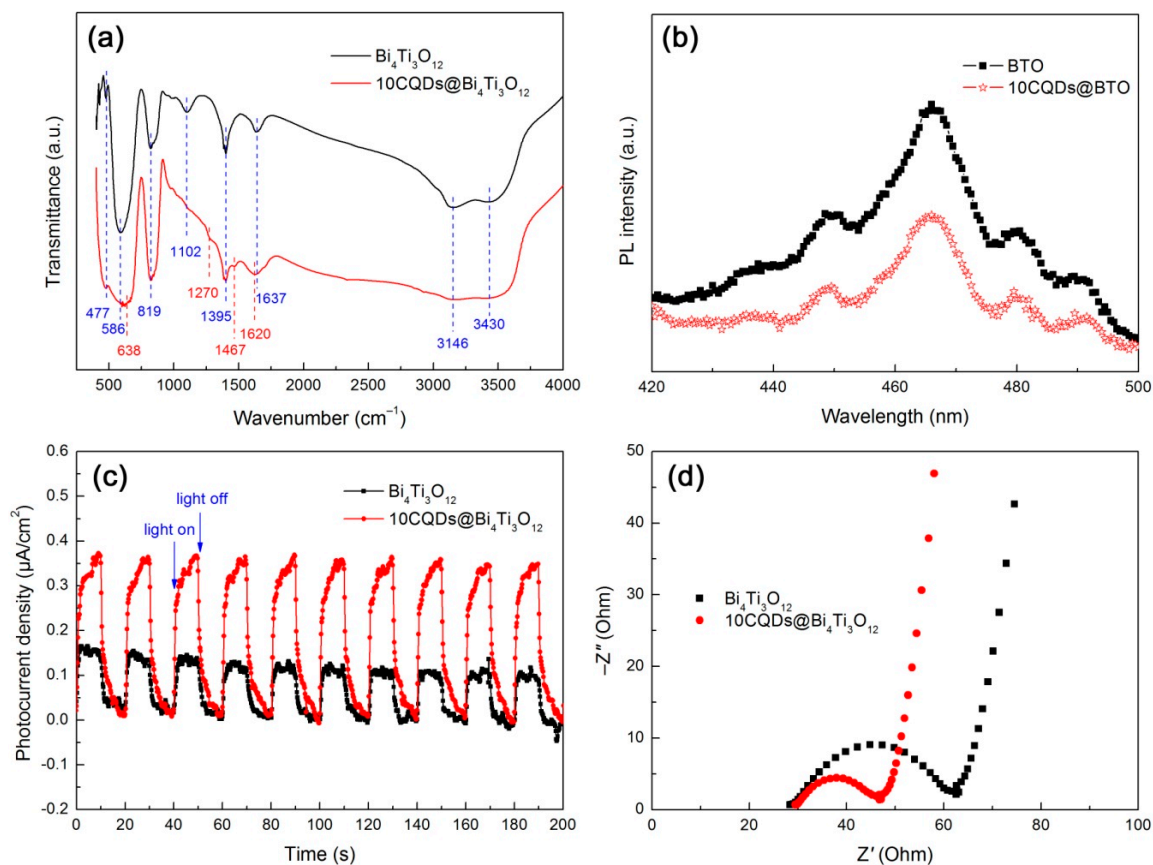


Figure 9. FTIR spectra (a), PL spectra (b), transient photocurrent response curves under intermittent irradiation of simulated sunlight (c) and Nyquist plots of the EIS spectra under simulated sunlight irradiation (d) of $\text{Bi}_4\text{Ti}_3\text{O}_{12}$ and $10\text{CQDs}@ \text{Bi}_4\text{Ti}_3\text{O}_{12}$.

Figure 9c shows the transient photocurrent response curves of $\text{Bi}_4\text{Ti}_3\text{O}_{12}$ and $10\text{CQDs}@ \text{Bi}_4\text{Ti}_3\text{O}_{12}$ measured under intermittent irradiation of simulated sunlight with 10 min irradiation followed by 10 min intervals. When the simulated sunlight is turned off, a photocurrent density of ca. 0.10–0.16 and 0.34–0.37 $\mu\text{A}\cdot\text{cm}^{-2}$ is observed for bare $\text{Bi}_4\text{Ti}_3\text{O}_{12}$ and $10\text{CQDs}@ \text{Bi}_4\text{Ti}_3\text{O}_{12}$, respectively. The photocurrent density for both samples immediately drops almost to zero when the light is turned off. This effect appears to be very reproducible upon alternately turning on and off the light. The transient photocurrent measurement clearly demonstrates that the $10\text{CQDs}@ \text{Bi}_4\text{Ti}_3\text{O}_{12}$ composite exhibits a more efficient separation of photogenerated electron/hole pairs than bare $\text{Bi}_4\text{Ti}_3\text{O}_{12}$. This result is further confirmed by the Nyquist plots of the EIS spectra, as shown in Figure 9d. It is clearly seen that the Nyquist plots of both samples display a semicircle (high-frequency region) followed by a straight line (low-frequency region). However, a smaller semicircle diameter is observed for the composite. It is well established that the semicircle diameter of the Nyquist plots is correlated with the charge-transfer resistance at the electrode/electrolyte interface, and a smaller diameter suggests a smaller charge-transfer resistance [66,67]. The EIS spectrum analysis elucidates an enhanced electron/hole pair separation and interface charge transfer under irradiation of simulated sunlight for the $10\text{CQDs}@ \text{Bi}_4\text{Ti}_3\text{O}_{12}$ composite.

Based on the aforementioned experimental results and analyses, a possible photocatalytic mechanism of CQDs@Bi₄Ti₃O₁₂ toward the dye degradation is proposed, as schematically illustrated in Figure 10. Under simulated sunlight irradiation, electrons are excited from the valence band (VB) of Bi₄Ti₃O₁₂ to its CB, thus creating electron/hole pairs. Simultaneously, the electronic excitation process also occurs in CQDs, i.e., electrons in the π orbital or σ orbital of CQDs are excited to a high-energy state such as the lowest unoccupied molecular orbital (LUMO) [19]. The photoexcited CQDs are excellent electron donors and electron acceptors. As a result, the CB electrons in Bi₄Ti₃O₁₂ will transfer to the π orbital or σ orbital of CQDs. Conversely, the photoexcited electrons in CQDs can be also transferred to the CB of Bi₄Ti₃O₁₂. The interesting electron transfer process can efficiently suppress the recombination of photogenerated electron/hole pairs in Bi₄Ti₃O₁₂. Consequently, more photogenerated carriers are able to participate in the photocatalytic reactions, thus leading to an increased photocatalytic performance of the CQDs@Bi₄Ti₃O₁₂ composites under simulated sunlight irradiation. It is noted that the Bi₄Ti₃O₁₂ square plates have a bandgap of 3.33 eV, implying that bare Bi₄Ti₃O₁₂ plates exhibit a poor photocatalytic activity under visible light irradiation. However, when CQDs are decorated on Bi₄Ti₃O₁₂, the obtained CQDs@Bi₄Ti₃O₁₂ composites manifest an obviously enhanced visible-light photocatalytic activity toward the dye degradation, as shown in Figure 4c,d. This phenomenon can be attributed to the following reasons. Under visible light irradiation, the π electrons in CQDs could be excited to the LUMO. When the electrons fall back to the σ orbital, an up-conversion photoluminescence is emitted [19]. The up-conversion photoluminescence could have photon energy larger than the bandgap energy of Bi₄Ti₃O₁₂ and would induce the electron excitation from the VB to the CB of Bi₄Ti₃O₁₂. The PL-induced electrons and holes are able to participate in the photocatalytic reactions. On the other hand, the photoexcited electrons in CQDs could also participate in the photocatalytic reactions. The two factors collectively result in the enhanced visible-light photocatalytic activity of the CQDs@Bi₄Ti₃O₁₂ composites.

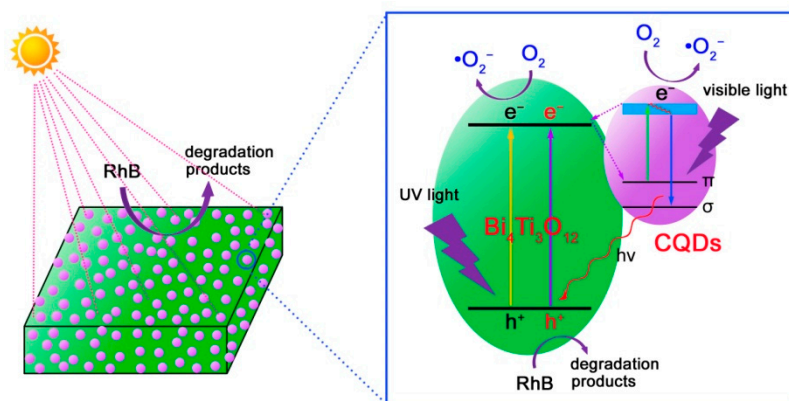


Figure 10. Schematic illustration of the photocatalytic mechanism of CQDs@Bi₄Ti₃O₁₂ for the dye degradation under simulated sunlight irradiation.

Reactive species trapping experiments were carried out to reveal their role in the degradation of RhB over 10CQDs@Bi₄Ti₃O₁₂. In this study, ethanol, benzoquinone (BQ) and ammonium oxalate (AO) were used as the scavengers of hydroxyl ($\bullet\text{OH}$), superoxide ($\bullet\text{O}_2^-$) and photogenerated h⁺, respectively [68]. Figure 11a shows the effect of ethanol (5 mL), BQ (0.1 mmol) and AO (0.1 mmol) on the degradation percentage of RhB at 120 min of photocatalysis. It is seen that the addition of ethanol to the reaction solution has almost no effect on the dye degradation, implying a minor or negligible role of $\bullet\text{OH}$ in the dye degradation. The addition of BQ leads to a slight suppression of the dye degradation. This suggests that the role of $\bullet\text{O}_2^-$ cannot be neglected, but it plays only a slight role in the photocatalytic reaction. With the addition of AO, however, the dye degradation is significantly suppressed and only 19.7% of RhB is observed to be degraded. This indicates that the photogenerated h⁺ is the dominant active species responsible for the dye degradation. To reveal the CB and VB

potentials of $\text{Bi}_4\text{Ti}_3\text{O}_{12}$ square plates, we carried out the Mott–Schottky measurement according to the method described in the literature [69–71], as shown in Figure 11b. By extrapolating the linear portion of the Mott–Schottky plot to the V axis, the flat band potential (V_{FB}) is obtained as -0.75 V vs SCE. The SCE potential can be converted to the potential against a normal hydrogen electrode (NHE) using $V(\text{NHE}) = V(\text{SCE}) + 0.059\text{pH} + 0.242$ (here $\text{pH} = 7$) [71]. The positive slope of the Mott–Schottky plot suggests that $\text{Bi}_4\text{Ti}_3\text{O}_{12}$ exhibits an n-type semiconductivity. Assuming that the gap between the flat band potential and the CB edge is negligible for an n-type semiconductor, the CB potential of $\text{Bi}_4\text{Ti}_3\text{O}_{12}$ square plates is therefore estimated as -0.10 V vs NHE. Their VB potential is obtained as $+3.23$ V vs NHE using $V_{\text{VB}} = V_{\text{CB}} - E_g$ ($E_g = 3.33$ V). It is noted that the VB potential of $\text{Bi}_4\text{Ti}_3\text{O}_{12}$ is more positive than the redox potentials of $\text{H}_2\text{O}/\bullet\text{OH}$ ($+2.38$ V vs NHE) and $\text{OH}^-/\bullet\text{OH}$ ($+1.99$ V vs NHE) [72]. However, the reactive species trapping experiments demonstrate that $\bullet\text{OH}$ plays a negligible role in the dye degradation. To further confirm this, we also measured $\bullet\text{OH}$ radicals by PL spectroscopy using terephthalic acid as a probe of $\bullet\text{OH}$, as described in the literature [72]. Nevertheless, no $\bullet\text{OH}$ radicals are detected in the $10\text{CQDs}@ \text{Bi}_4\text{Ti}_3\text{O}_{12}$ photocatalytic system. The generation of minor $\bullet\text{O}_2^-$ radicals could be derived from the reaction of adsorbed O_2 molecules with the photoexcited electrons in CQDs or photogenerated electrons at higher excited states of $\text{Bi}_4\text{Ti}_3\text{O}_{12}$.

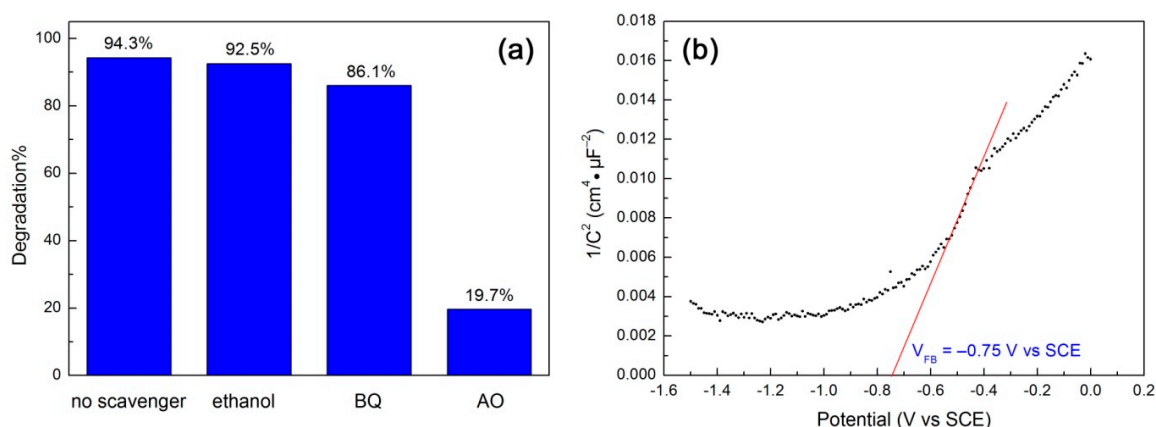


Figure 11. (a) Effect of ethanol, BQ and AO on the degradation percentage of RhB at 120 min of photocatalysis. (b) Mott–Schottky plot of $\text{Bi}_4\text{Ti}_3\text{O}_{12}$ square plates obtained at 5000 Hz.

4. Conclusions

A hydrothermal route was used to synthesize $\text{Bi}_4\text{Ti}_3\text{O}_{12}$ square plates with an average lateral size of ~ 1 μm and average thickness of ~ 200 nm. The growth process of the square plates was systematically investigated. CQDs derived from glucose were assembled on the surface of $\text{Bi}_4\text{Ti}_3\text{O}_{12}$ square plates via a hydrothermal route. Compared to bare $\text{Bi}_4\text{Ti}_3\text{O}_{12}$, the as-prepared $\text{CQDs}@ \text{Bi}_4\text{Ti}_3\text{O}_{12}$ composites with an appropriate amount of CQDs manifest an increased photocatalytic performance for the RhB degradation under irradiation of simulated sunlight and visible light. The optimal $\text{CQDs}@ \text{Bi}_4\text{Ti}_3\text{O}_{12}$ composite photocatalyzes 94.3% removal of the dye under simulated sunlight irradiation, demonstrating a photocatalytic activity ca. 1.8 times higher than that of bare $\text{Bi}_4\text{Ti}_3\text{O}_{12}$. The enhanced photocatalytic performance of CQDs-modified $\text{Bi}_4\text{Ti}_3\text{O}_{12}$ is mainly attributed to the efficient separation of photogenerated electron/hole pairs and increased visible light absorption. The efficient utilization of visible light during the photocatalysis is manifested in 2 aspects: (1) The visible-light photoexcited electrons in CQDs could participate in the photocatalytic reactions, and (2) additional electron/hole pairs in $\text{Bi}_4\text{Ti}_3\text{O}_{12}$ could be generated by the up-conversion photoluminescence emitted from CQDs.

Author Contributions: H.Y. conceived the idea of experiment; X.Z. and Z.M.C. performed the experiments; H.Y., X.Z., Z.M.C., X.X.W. and Z.Y. discussed the results; H.Y. wrote the manuscript; all authors read and approved the final manuscript.

Acknowledgments: This work was supported by the National Natural Science Foundation of China (Grant No. 51662027) and the HongLiu First-Class Disciplines Development Program of Lanzhou University of Technology.

Conflicts of Interest: The authors declare that they have no competing interests.

References

1. Moroz, P.; Boddy, A.; Zamkov, M. Challenges and prospects of photocatalytic applications utilizing semiconductor nanocrystals. *Front. Chem.* **2018**, *6*, 353. [[CrossRef](#)] [[PubMed](#)]
2. Di, L.J.; Yang, H.; Xian, T.; Chen, X.J. Enhanced photocatalytic activity of NaBH₄ reduced BiFeO₃ nanoparticles for rhodamine B decolorization. *Materials* **2017**, *10*, 1118. [[CrossRef](#)] [[PubMed](#)]
3. Xia, Y.M.; He, Z.M.; Yang, W.; Tang, B.; Lu, Y.L.; Hu, K.J.; Su, J.B.; Li, X.P. Effective charge separation in BiOI/Cu₂O composites with enhanced photocatalytic activity. *Mater. Res. Express* **2018**, *5*, 025504. [[CrossRef](#)]
4. Wang, S.F.; Gao, H.J.; Wei, Y.; Li, Y.W.; Yang, X.H.; Fang, L.M.; Lei, L. Insight into the optical, color, photoluminescence properties, and photocatalytic activity of the N-O and C-O functional groups decorating spinel type magnesium aluminate. *CrystEngComm* **2019**. [[CrossRef](#)]
5. Zangeneh, H.; Zinatizadeh, A.A.L.; Habibi, M.; Akia, M.; Isa, M.H. Photocatalytic oxidation of organic dyes and pollutants in wastewater using different modified titanium dioxides: A comparative review. *J. Ind. Eng. Chem.* **2015**, *26*, 1–36. [[CrossRef](#)]
6. Zhao, W.H.; Wei, Z.Q.; Zhang, L.; Wu, X.J.; Wang, X. Cr doped SnS₂ nanoflowers: Preparation, characterization and photocatalytic decolorization. *Mater. Sci. Semicond. Process.* **2018**, *88*, 173–180. [[CrossRef](#)]
7. Ariyanti, D.; Mills, L.; Dong, J.; Yao, Y.; Gao, W. NaBH₄ modified TiO₂: Defect site enhancement related to its photocatalytic activity. *Mater. Chem. Phys.* **2017**, *199*, 571–576. [[CrossRef](#)]
8. Yan, Y.X.; Yang, H.; Zhao, X.X.; Li, R.S.; Wang, X.X. Enhanced photocatalytic activity of surface disorder-engineered CaTiO₃. *Mater. Res. Bull.* **2018**, *105*, 286–290. [[CrossRef](#)]
9. Tayyebi, A.; Soltani, T.; Hong, H.; Lee, B.K. Improved photocatalytic and photoelectrochemical performance of monoclinic bismuth vanadate by surface defect states (Bi_{1-x}VO₄). *J. Colloid Interface Sci.* **2018**, *514*, 565–575. [[CrossRef](#)]
10. Dutta, D.P.; Tyagi, A.K. Facile sonochemical synthesis of Ag modified Bi₄Ti₃O₁₂ nanoparticles with enhanced photocatalytic activity under visible light. *Mater. Res. Bull.* **2016**, *74*, 397–407. [[CrossRef](#)]
11. Wang, F.; Yang, H.; Zhang, Y.C. Enhanced photocatalytic performance of CuBi₂O₄ particles decorated with Ag nanowires. *Mater. Sci. Semicond. Proc.* **2018**, *73*, 58–66. [[CrossRef](#)]
12. Wang, H.L.; Zhang, L.S.; Chen, Z.G.; Hu, J.Q.; Li, S.J.; Wang, Z.H.; Liu, J.S.; Wang, X.C. Semiconductor heterojunction photocatalysts: design, construction, and photocatalytic performances. *Chem. Soc. Rev.* **2014**, *43*, 5234–5244. [[CrossRef](#)] [[PubMed](#)]
13. Guerrero-Araque, D.; Ramirez-Ortega, D.; Acevedo-Pena, P.; Tzompantzi, F.; Calderon, H.A.; Gomez, R. Interfacial charge-transfer process across ZrO₂-TiO₂ heterojunction and its impact on photocatalytic activity. *J. Photochem. Photobiol. A-Chem.* **2017**, *335*, 276–286. [[CrossRef](#)]
14. Zeng, Y.; Chen, X.F.; Yi, Z.; Yi, Y.G.; Xu, X.B. Fabrication of p-n heterostructure ZnO/Si moth-eye structures: Antireflection, enhanced charge separation and photocatalytic properties. *Appl. Surf. Sci.* **2018**, *441*, 40–48. [[CrossRef](#)]
15. Xia, Y.; He, Z.; Su, J.; Liu, Y.; Tang, B. Fabrication and photocatalytic property of novel SrTiO₃/Bi₅O₇I nanocomposites. *Nanoscale Res. Lett.* **2018**, *13*, 148. [[CrossRef](#)] [[PubMed](#)]
16. Di, L.J.; Yang, H.; Xian, T.; Chen, X.J. Construction of Z-scheme g-C₃N₄/CNT/Bi₂Fe₄O₉ composites with improved simulated-sunlight photocatalytic activity for the dye degradation. *Micromachines* **2018**, *9*, 613. [[CrossRef](#)] [[PubMed](#)]
17. Fernando, K.A.S.; Sahu, S.P.; Liu, Y.; Lewis, W.K.; Gulians, E.; Jafariyan, A.; Wang, P.; Bunker, C.E.; Sun, Y.P. Carbon quantum dots and applications in photocatalytic energy conversion. *ACS Appl. Mater. Interfaces* **2015**, *7*, 8363–8376. [[CrossRef](#)]
18. Yu, H.J.; Shi, R.; Zhao, Y.F.; Waterhouse, G.I.N.; Wu, L.Z.; Tung, C.H.; Zhang, T.R. Smart utilization of carbon dots in semiconductor photocatalysis. *Adv. Mater.* **2016**, *28*, 9454–9477. [[CrossRef](#)]
19. Li, H.T.; Kang, Z.H.; Liu, Y.; Lee, S.T. Carbon nanodots: Synthesis, properties and applications. *J. Mater. Chem.* **2012**, *22*, 24230–24253. [[CrossRef](#)]

20. Devi1, P.; Thakur, A.; Bhardwaj, S.K.; Saini, S.; Rajput, P.; Kumar, P. Metal ion sensing and light activated antimicrobial activity of aloe vera derived carbon dots. *J. Mater. Sci.-Mater. Electron.* **2018**, *29*, 17254–17261. [[CrossRef](#)]
21. Yang, Y.N.; Xia, L.; Zhang, T.; Shi, B.; Huang, L.N.; Zhong, B.; Zhang, X.Y.; Wang, H.T.; Zhang, J.; Wen, G.W. Fe₃O₄@LAS/RGO composites with a multiple transmission-absorption mechanism and enhanced electromagnetic wave absorption performance. *Chem. Eng. J.* **2018**, *352*, 510–518. [[CrossRef](#)]
22. Jiang, J.L.; He, X.X.; Du, J.F.; Pang, X.J.; Yang, H.; Wei, Z.Q. In-situ fabrication of graphene-nickel matrix composites. *Mater. Lett.* **2018**, *220*, 178–181. [[CrossRef](#)]
23. Liang, C.P.; Niu, G.; Chen, X.F.; Zhou, Z.G.; Yi, Z.; Ye, X.; Duan, T.; Yi, Y.; Xiao, S.Y. Tunable triple-band graphene refractive index sensor with good angle-polarization tolerance. *Opt. Commun.* **2019**, *436*, 57–62. [[CrossRef](#)]
24. Cen, C.L.; Lin, H.; Huang, J.; Liang, C.P.; Chen, X.F.; Tang, Y.J.; Yi, Z.; Ye, X.; Liu, J.W.; Yi, Y.G.; et al. A tunable plasmonic refractive index sensor with nanoring-strip graphene arrays. *Sensors* **2018**, *18*, 4489. [[CrossRef](#)] [[PubMed](#)]
25. Wang, X.X.; Wu, X.X.; Chen, Y.Z.; Bai, X.L.; Pang, Z.Y.; Yang, H.; Qi, Y.P.; Wen, X.L. Investigation of wide-range refractive index sensor based on asymmetric metal-cladding dielectric waveguide structure. *AIP Adv.* **2018**, *8*, 105029. [[CrossRef](#)]
26. Pang, Z.Y.; Tong, H.; Wu, X.X.; Zhu, J.K.; Wang, X.X.; Yang, H.; Qi, Y.P. Theoretical study of multiexposure zeroth-order waveguide mode interference lithography. *Opt. Quant. Electron.* **2018**, *50*, 335. [[CrossRef](#)]
27. Wang, X.X.; Pang, Z.Y.; Tong, H.; Wu, X.X.; Bai, X.L.; Yang, H.; Wen, X.L.; Qi, Y.P. Theoretical investigation of subwavelength structure fabrication based on multi-exposure surface plasmon interference lithography. *Results Phys.* **2019**, *12*, 732–737. [[CrossRef](#)]
28. Xia, L.; Zhang, X.Y.; Yang, Y.N.; Zhang, J.; Zhong, B.; Zhang, T.; Wang, H.T. Enhanced electromagnetic wave absorption properties of laminated SiCNW-C_f/lithium-aluminum-silicate (LAS) composites. *J. Alloys Compd.* **2018**, *748*, 154–162. [[CrossRef](#)]
29. Sharma, S.; Mehta, S.K.; Ibhaddon, A.O.; Kansal, S.K. Fabrication of novel carbon quantum dots modified bismuth oxide (α -Bi₂O₃/C-dots): Material properties and catalytic applications. *J. Colloid Interface Sci.* **2019**, *533*, 227–237. [[CrossRef](#)]
30. Di, J.; Xia, J.X.; Ge, Y.P.; Li, H.P.; Ji, H.Y.; Xu, H.; Zhang, Q.; Li, H.M.; Li, M.N. Novel visible-light-driven CQDs/Bi₂WO₆ hybrid materials with enhanced photocatalytic activity toward organic pollutants degradation and mechanism insight. *Appl. Catal. B-Environ.* **2015**, *168–169*, 51–61. [[CrossRef](#)]
31. Duo, F.F.; Wang, Y.W.; Fan, C.M.; Zhang, X.C.; Wang, Y.F. Enhanced visible light photocatalytic activity and stability of CQDs/BiOBr composites: The upconversion effect of CQDs. *J. Alloy Compd.* **2016**, *685*, 34–41. [[CrossRef](#)]
32. Hong, Y.Z.; Meng, Y.D.; Zhang, G.Y.; Yin, B.X.; Zhao, Y.; Shi, W.D.; Li, C.S. Facile fabrication of stable metal-free CQDs/g-C₃N₄ heterojunctions with efficiently enhanced visible-light photocatalytic activity. *Sep. Purif. Technol.* **2016**, *171*, 229–237. [[CrossRef](#)]
33. Zhao, X.X.; Yang, H.; Li, S.H.; Cui, Z.M.; Zhang, C.R. Synthesis and theoretical study of large-sized Bi₄Ti₃O₁₂ square nanosheets with high photocatalytic activity. *Mater. Res. Bull.* **2018**, *107*, 180–188. [[CrossRef](#)]
34. Zhang, Y.Z.; Chen, Z.W.; Lu, Z.Y. A facile method for the preparation of colored Bi₄Ti₃O_{12-x} nanosheets with enhanced visible-light photocatalytic hydrogen evolution activity. *Nanomaterials* **2018**, *8*, 261. [[CrossRef](#)] [[PubMed](#)]
35. Gao, X.M.; Dai, Y.; Zhang, Y.; Wang, Z.H.; Fu, F. Preparation and photocatalytic performance of spherical-like Bi₄Ti₃O₁₂ composite. *Chin. J. Inorg. Chem.* **2017**, *33*, 455–462.
36. Qian, K.; Jiang, Z.F.; Shi, H.; Wei, W.; Zhu, C.Z.; Xie, J.M. Constructing mesoporous Bi₄Ti₃O₁₂ with enhanced visible light photocatalytic activity. *Mater. Lett.* **2016**, *183*, 303–306. [[CrossRef](#)]
37. Zhao, W.; Jia, Z.; Lei, E.; Wang, L.G.; Li, Z.Y.; Dai, Y.J. Photocatalytic degradation efficacy of Bi₄Ti₃O₁₂ micro-scale platelets over methylene blue under visible light. *J. Phys. Chem. Solids* **2013**, *74*, 1604–1607. [[CrossRef](#)]
38. Hervoches, C.H.; Lightfoot, P. A variable-temperature powder neutron diffraction study of ferroelectric Bi₄Ti₃O₁₂. *Chem. Mater.* **1999**, *11*, 3359–3364. [[CrossRef](#)]
39. Cummins, S.E.; Cross, L.E. Electrical and optical properties of ferroelectric Bi₄Ti₃O₁₂ single crystals. *J. Appl. Phys.* **1968**, *39*, 2268. [[CrossRef](#)]

40. Cui, Z.M.; Yang, H.; Zhao, X.X. Enhanced photocatalytic performance of g-C₃N₄/Bi₄Ti₃O₁₂ heterojunction. *Mater. Sci. Eng. B* **2018**, *229*, 160–172. [[CrossRef](#)]
41. Zhao, Y.W.; Fan, H.Q.; Fu, K.; Ma, L.T.; Li, M.M.; Fang, J.W. Intrinsic electric field assisted polymeric graphitic carbon nitride coupled with Bi₄Ti₃O₁₂/Bi₂Ti₂O₇ heterostructure nanofibers toward enhanced photocatalytic hydrogen evolution. *Int. J. Hydrogen Energy* **2016**, *41*, 16913–16926. [[CrossRef](#)]
42. Hou, D.F.; Hu, X.L.; Hu, P.; Zhang, W.; Zhang, M.F.; Huang, Y.H. Bi₄Ti₃O₁₂ nanofibers–BiOI nanosheets p–n junction: facile synthesis and enhanced visible-light photocatalytic activity. *Nanoscale* **2013**, *5*, 9764–9772. [[CrossRef](#)]
43. Shi, B.T.; Yin, H.Y.; Gong, J.Y.; Nie, Q.L. A novel p–n heterojunction of Ag₂O/Bi₄Ti₃O₁₂ nanosheet with exposed (001) facets for enhanced visible-light-driven photocatalytic activity. *Mater. Lett.* **2017**, *201*, 74–77. [[CrossRef](#)]
44. Liu, Y.B.; Zhu, G.Q.; Gao, J.Z.; Hojamberdiev, M.; Lu, H.B.; Zhu, R.L.; Wei, X.M.; Liu, P. A novel CeO₂/Bi₄Ti₃O₁₂ composite heterojunction structure with an enhanced photocatalytic activity for bisphenol A. *J. Alloy Compd.* **2016**, *688*, 487–496. [[CrossRef](#)]
45. Zhao, W.; Wang, H.X.; Feng, X.N.; Jiang, W.Y.; Zhao, D.; Li, J.Y. Hydrothermal synthesis and photocatalytic activities of Bi₄Ti₃O₁₂/SrTiO₃ composite micro-platelets. *Mater. Res. Bull.* **2015**, *70*, 179–183. [[CrossRef](#)]
46. Zheng, C.X.; Yang, H.; Cui, Z.M.; Zhang, H.M.; Wang, X.X. A novel Bi₄Ti₃O₁₂/Ag₃PO₄ heterojunction photocatalyst with enhanced photocatalytic performance. *Nanoscale Res. Lett.* **2017**, *12*, 608. [[CrossRef](#)]
47. Liu, Y.; Zhang, M.Y.; Li, L.; Zhang, X.T. In situ ion exchange synthesis of the Bi₄Ti₃O₁₂/Bi₂S₃ heterostructure with enhanced photocatalytic activity. *Catal. Commun.* **2015**, *60*, 23–26. [[CrossRef](#)]
48. Cao, T.P.; Li, Y.J.; Wang, C.H.; Zhang, Z.Y.; Zhang, M.Y.; Shao, C.L.; Liu, Y.C. Bi₄Ti₃O₁₂ nanosheets/TiO₂ submicron fibers heterostructures: in situ fabrication and high visible light photocatalytic activity. *J. Mater. Chem.* **2011**, *21*, 6922–6927. [[CrossRef](#)]
49. Wang, T.; Liu, X.Q.; Ma, C.C.; Zhu, Z.; Liu, Y.; Liu, Z.; Wei, M.B.; Zhao, X.X.; Dong, H.J.; Huo, P.W.; et al. Bamboo prepared carbon quantum dots (CQDs) for enhancing Bi₃Ti₄O₁₂ nanosheets photocatalytic activity. *J. Alloy Compd.* **2018**, *752*, 106–114. [[CrossRef](#)]
50. Dai, J.Y.; Li, J.J.; Zhang, Q.B.; Liao, M.; Duan, T.; Yao, W.T. Co₃S₄@C@MoS₂ microstructures fabricated from MOF template as advanced lithium-ion battery anode. *Mater. Lett.* **2019**, *236*, 483–486. [[CrossRef](#)]
51. Zheng, C.X.; Yang, H. Assembly of Ag₃PO₄ nanoparticles on rose flower-like Bi₂WO₆ hierarchical architectures for achieving high photocatalytic performance. *J. Mater. Sci.-Mater. Electron.* **2018**, *29*, 9291–9300. [[CrossRef](#)]
52. Eckert, J.O., Jr.; Hung-Houston, C.C.; Gersten, B.L.; Lencka, M.M.; Riman, R.E. Kinetics and mechanisms of hydrothermal synthesis of barium titanate. *J. Am. Ceram. Soc.* **1996**, *79*, 2929–2939. [[CrossRef](#)]
53. Konstantinou, I.K.; Albanis, T.A. TiO₂-assisted photocatalytic degradation of azo dyes in aqueous solution: kinetic and mechanistic investigations: A review. *Appl. Catal. B-Environ.* **2004**, *49*, 1–14. [[CrossRef](#)]
54. Zhao, X.X.; Yang, H.; Li, R.S.; Cui, Z.M.; Liu, X.Q. Synthesis of heterojunction photocatalysts composed of Ag₂S quantum dots combined with Bi₄Ti₃O₁₂ nanosheets for the degradation of dyes. *Environ. Sci. Pollut. Res. Int.* **2019**, in press. [[CrossRef](#)]
55. Di, L.J.; Yang, H.; Xian, T.; Chen, X.J. Facile synthesis and enhanced visible-light photocatalytic activity of novel p-Ag₃PO₄/n-BiFeO₃ heterojunction composites for dye degradation. *Nanoscale Res. Lett.* **2018**, *13*, 257. [[CrossRef](#)]
56. Shi, B.; Yin, H.; Gong, J.; Nie, Q. Ag/AgCl decorated Bi₄Ti₃O₁₂ nanosheet with highly exposed (001) facets for enhanced photocatalytic degradation of Rhodamine B, Carbamazepine and Tetracycline. *Appl. Surf. Sci.* **2017**, *419*, 614–623. [[CrossRef](#)]
57. Du, C.; Li, D.H.; He, Q.Y.; Liu, J.M.; Li, W.; He, G.N.; Wang, Y.Z. Design and simple synthesis of composite Bi₁₂TiO₂₀/Bi₄Ti₃O₁₂ with a good photocatalytic quantum efficiency and high production of photo-generated hydroxyl radicals. *Phys. Chem. Chem. Phys.* **2016**, *18*, 26530–26538. [[CrossRef](#)]
58. Lin, H.; Ye, X.; Chen, X.F.; Zhou, Z.G.; Yi, Z.; Niu, G.; Yi, Y.G.; Hua, Y.T.; Hua, J.J.; Xiao, S.Y. Plasmonic absorption enhancement in graphene circular and elliptical disk arrays. *Mater. Res. Express* **2019**. [[CrossRef](#)]
59. Yan, Y.X.; Yang, H.; Zhao, X.X.; Zhang, H.M.; Jiang, J.L. A hydrothermal route to the synthesis of CaTiO₃ nanocuboids using P25 as the titanium source. *J. Electron. Mater.* **2018**, *47*, 3045–3050. [[CrossRef](#)]
60. Yu, B.Y.; Kwak, S.Y. Carbon quantum dots embedded with mesoporous hematite nanospheres as efficient visible light-active photocatalysts. *J. Mater. Chem.* **2012**, *22*, 8345–8353. [[CrossRef](#)]

61. Wang, S.F.; Gao, H.J.; Fang, L.M.; Wei, Y.; Li, Y.W.; Lei, L. Synthesis and characterization of BaAl₂O₄ catalyst and its photocatalytic activity towards degradation of methylene blue dye. *Z. Phys. Chem.* **2019**. [[CrossRef](#)]
62. Mert, B.D.; Mert, M.E.; Kardas, G.; Yazici, B. Experimental and theoretical studies on electrochemical synthesis of poly(3-amino-1,2,4-triazole). *Appl. Surf. Sci.* **2012**, *258*, 9668–9674. [[CrossRef](#)]
63. Ganesh, R.S.; Sharma, S.K.; Abinnas, N.; Durgadevi, E.; Raji, P.; Ponnusamy, S.; Muthamizhchelvan, C.; Hayakawa, Y.; Kim, D.Y. Fabrication of the flexible nanogenerator from BTO nanopowders on graphene coated PMMA substrates by sol-gel method. *Mater. Chem. Phys.* **2017**, *192*, 274–281. [[CrossRef](#)]
64. Dias, J.A.; Oliveira, J.A.; Renda, C.G.; Morelli, M.R. Production of nanometric Bi₄Ti₃O₁₂ powders: From synthesis to optical and dielectric properties. *Mater. Res.* **2018**, *21*, e20180118. [[CrossRef](#)]
65. Xie, R.Y.; Zhang, L.P.; Liu, H.C.; Xu, H.; Zhong, Y.; Sui, X.F.; Mao, Z.P. Construction of CQDs-Bi₂₀TiO₃₂/PAN electrospun fiber membranes and their photocatalytic activity for isoproturon degradation under visible light. *Mater. Res. Bull.* **2017**, *94*, 7–14. [[CrossRef](#)]
66. Xia, Y.M.; He, Z.M.; Lu, Y.L.; Tang, B.; Sun, S.P.; Su, J.B.; Li, X.P. Fabrication and photocatalytic property of magnetic SrTiO₃/NiFe₂O₄ heterojunction nanocomposites. *RSC Adv.* **2018**, *8*, 5441–5450. [[CrossRef](#)]
67. Zhu, X.L.; Wei, Z.Q.; Zhao, W.H.; Zhang, X.D.; Zhang, L.; Wang, X. Microstructure and electrochemical properties of ZnMn₂O₄ nanopowder synthesized using different surfactants. *J. Electron. Mater.* **2018**, *47*, 6428–6436. [[CrossRef](#)]
68. Ye, Y.C.; Yang, H.; Wang, X.X.; Feng, W.J. Photocatalytic, Fenton and photo-Fenton degradation of RhB over Z-scheme g-C₃N₄/LaFeO₃ heterojunction photocatalysts. *Mater. Sci. Semicond. Proc.* **2018**, *82*, 14–24. [[CrossRef](#)]
69. Fattah-alhosseini, A. Passivity of AISI 321 stainless steel in 0.5 M H₂SO₄ solution studied by Mott–Schottky analysis in conjunction with the point defect model. *Arab. J. Chem.* **2016**, *9*, S1342–S1348. [[CrossRef](#)]
70. Cardon, F.; Gomes, W.P. On the determination of the flat-band potential of a semiconductor in contact with a metal or an electrolyte from the Mott-Schottky plot. *J. Phys. D Appl. Phys.* **1978**, *11*, L63–L67. [[CrossRef](#)]
71. Wang, F.; Yang, H.; Zhang, H.M.; Jiang, J.L. Growth process and enhanced photocatalytic performance of CuBi₂O₄ hierarchical microcuboids decorated with AuAg alloy nanoparticles. *J. Mater. Sci.-Mater. Electron.* **2018**, *29*, 1304–1316. [[CrossRef](#)]
72. Ye, Y.C.; Yang, H.; Zhang, H.M.; Jiang, J.L. A promising Ag₂CrO₄/LaFeO₃ heterojunction photocatalyst applied to photo-Fenton degradation of RhB. *Environ. Technol.* **2019**. [[CrossRef](#)] [[PubMed](#)]



© 2019 by the authors. Licensee MDPI, Basel, Switzerland. This article is an open access article distributed under the terms and conditions of the Creative Commons Attribution (CC BY) license (<http://creativecommons.org/licenses/by/4.0/>).